



HAL
open science

Hyperfine excitation of NH and ND by molecular hydrogen

Paul Pirlot Jankowiak, François Lique, Javier R. Goicoechea

► **To cite this version:**

Paul Pirlot Jankowiak, François Lique, Javier R. Goicoechea. Hyperfine excitation of NH and ND by molecular hydrogen: Rate coefficients and astrophysical modeling. *Astronomy and Astrophysics - A&A*, 2024, 683, pp.A155. 10.1051/0004-6361/202348865 . hal-04507157

HAL Id: hal-04507157

<https://hal.science/hal-04507157>

Submitted on 15 Mar 2024

HAL is a multi-disciplinary open access archive for the deposit and dissemination of scientific research documents, whether they are published or not. The documents may come from teaching and research institutions in France or abroad, or from public or private research centers.

L'archive ouverte pluridisciplinaire **HAL**, est destinée au dépôt et à la diffusion de documents scientifiques de niveau recherche, publiés ou non, émanant des établissements d'enseignement et de recherche français ou étrangers, des laboratoires publics ou privés.



Distributed under a Creative Commons Attribution 4.0 International License

Hyperfine excitation of NH and ND by molecular hydrogen

Rate coefficients and astrophysical modeling

Paul Pirlot Jankowiak¹ , François Lique¹ , and Javier R. Goicoechea² 

¹ Univ. Rennes, CNRS, IPR (Institut de Physique de Rennes) – UMR 6251, 35000 Rennes, France
e-mail: paul.pirlot@univ-rennes.fr; francois.lique@univ-rennes.fr

² Instituto de Física Fundamental (CSIC), Calle Serrano 121-123, 28006 Madrid, Spain

Received 6 December 2023 / Accepted 8 January 2024

ABSTRACT

The NH and ND radicals are of key importance in the comprehension of nitrogen chemistry and the enhancement of deuterated molecules in the interstellar medium. Observations by space telescopes yield spectra that can resolve the fine and hyperfine structure of these radicals, a consequence of the electronic and magnetic interactions of nitrogen, hydrogen, and deuterium nuclei. Accurate rate coefficients, induced by collisions with H₂, are required to interpret spectra of these radicals. We report the first rate coefficients for fine and hyperfine transitions of NH and ND in collision with both ortho- and para-H₂. Based on a recent four-dimensional potential energy surface, fine-structure resolved cross sections and rate coefficients are computed with the time-independent close-coupling method over a temperature range of 5–300 K. Our calculations include the first 25 energy levels of NH and ND. Hyperfine resolved cross sections and rate coefficients are determined using the infinite-order sudden (IOS) approximation between 5 and 200 K for NH and 100 K for ND. We consider the first 71 and 105 energy levels of NH and ND, respectively. General propensity rules are discussed. We found a significant isotopic substitution effect in the rate coefficients. In addition, the rate coefficients for collisions with H₂ are larger than those with He by a factor of up to 5, leading to lower critical densities for collisional excitation with H₂ than He. The impact of the new set of collisional data has been investigated in simple radiative transfer models of the NH emission seen toward the Orion Bar and the ejecta of the η Carinae binary star. We observed significant differences by a factor of 5 between the presently determined column densities for NH compared to those from the literature using He as a collider.

Key words. astrochemistry – molecular data – molecular processes – radiative transfer – scattering

1. Introduction

Nitrogen hydrides are key species in the formation of complex nitrogen-bearing molecules observed in the interstellar medium (ISM; Gerin et al. 2016). An accurate determination of the abundances of these species is essential for understanding nitrogen chemistry, which remains a subject of ongoing exploration (Bacmann et al. 2016). Among nitrogen hydrides, the NH radical is of particular interest since it is an important intermediate in the synthesis of heavier molecules (Bacmann et al. 2010; Gerin et al. 2016). Observations of NH were first reported in comets (Swings et al. 1941) and stellar atmospheres (Schmitt 1969; Lambert & Beer 1972). Meyer & Roth (1991) detected NH in the ISM in ζ Per and HD 27778 diffuse clouds through the A³Π–X³Σ UV absorption band. The high rotational constant of NH leads to rotational lines in the submillimeter frequency range (≥ 1 THz), making ground-based observations not suitable for detecting rotational transitions. Thanks to the Infrared Space Observatory (ISO), Cernicharo et al. (2000) and Goicoechea et al. (2004) reported the first detection of far-infrared fine-structure components 2₃ → 1₂ and 2₂ → 1₁ toward the Sgr B2 dense molecular cloud.

From the first detection of NH, large divergences between the determined abundances from observations and those predicted by chemical models were pointed out (Wagenblast et al. 1993). The much higher spectral resolution observations with the heterodyne receiver HIFI on board the *Herschel* space telescope led to the suggestion that the formation of NH in cold

molecular clouds and prestellar cores may occur through dissociative recombination of N₂H⁺ (Hily-Blant et al. 2010; Dislaire et al. 2012; Le Gal et al. 2014) in addition to the well known N⁺ + H₂ reaction followed by dissociative recombination. Various models confirmed the poor understanding of the NH abundance and other nitrogen hydrides despite the many observations in the solar-mass Class 0 protostar IRAS 16293-2422 (Bacmann et al. 2010; Hily-Blant et al. 2010), in the H II region G10.6-0.4 (W31; Persson et al. 2012), the star-forming region W49N (Persson et al. 2012), the binary star η Carinae, and the Homunculus nebula (Gull et al. 2020). Goicoechea & Roncero (2022) recently detected NH emission lines toward the Orion Bar photodissociation region (PDR), where their modeling based on state-specific rate coefficients calculations for the N + H₂(ν) → NH + H reaction lead to an enhancement of the NH column density by a factor ~ 25 compared to chemical models using thermal rate coefficients and showing better agreement with observations. The study revealed the importance of UV-pumped vibrationally excited H₂ in the formation of NH in strongly UV-irradiated molecular clouds.

The deuterium fractionation is also a fundamental parameter of the study of the ISM. It is well known that the abundance ratio between a deuterated molecule and its hydrogenated counterpart can deviate by several orders of magnitude from the elemental ratio [D]/[H] $\sim 2 \times 10^{-5}$ (Linsky et al. 2006) depending on the molecule and on the source. High degrees of molecular deuteration have been observed in various cold environments (Ceccarelli et al. 1998; Caselli et al. 2003; Bacmann et al. 2003).

In this context, the study of the ND radical is of interest to infer the deuterium enhancement in the chemistry of nitrogen hydrides. Bacmann et al. (2010) reported the first detection of ND in IRAS 16293-2422 resolving the hyperfine multiplet of the $1 \rightarrow 0$ rotational line and deriving an abundance ratio $[\text{ND}]/[\text{NH}] \geq 30\%$. Bacmann et al. (2016) also detected ND toward the 16293E prestellar core and confirmed the high degree of deuteration of the NH radical.

At low densities, the determination of molecular abundances cannot be achieved assuming local thermodynamic equilibrium (LTE). The computation of reliable state-to-state rate coefficients of NH and ND induced by collisions with the main collider H_2 in molecular clouds is required. Interactions of the molecular electronic spin and nuclear spin of the nitrogen and the hydrogen or deuterium atoms to the molecular rotation leads to a large number of energy levels to consider in scattering calculations. In addition, the inclusion of the internal structure of H_2 requires a large number of channels to consider in quantum dynamical calculations that are not achievable with current computational resources. There are presently no collisional data reported about fine and hyperfine resolved rate coefficients for NH and ND in collision with both ortho- and para- H_2 . Because of this lack of data, Bacmann et al. (2016) used scaled NH/ND-He hyperfine rate coefficients computed by Dumouchel et al. (2012) to model molecular spectra. In addition, Goicoechea & Roncero (2022) scaled fine-structure NH-He rate coefficients from Toboła et al. (2011). These estimations of NH- H_2 rate coefficients may not be accurate enough, especially in the case of light hydrides. Hyperfine line-overlap and opacity effects may also lead to subtle radiative effects and anomalous hyperfine line emission (Goicoechea et al. 2022).

To date, only a few investigations have reported hyperfine resolved rate coefficients for collisions involving a molecule possessing two nonzero nuclear spins such as N_2H^+ -He (Daniel et al. 2005), NH/ND-He (Dumouchel et al. 2012), or $^{13}\text{CCH}/^{13}\text{CH}$ -para- H_2 (Pirlot Jankowiak et al. 2023). Because NH is detected in both cold and warm astrophysical environments, it is essential to take into account explicitly the internal structure of H_2 in the scattering calculations. This work aims to fill this objective by providing fine and hyperfine resolved rate coefficients for NH and ND in collisions with molecular hydrogen (both ortho- and para- H_2). Fine-structure calculations are achieved with the close-coupling (CC) method, while the infinite-order sudden (IOS) approximation (Faure & Lique 2012; Lanza & Lique 2014) is employed to overcome the computational challenges posed by the inclusion of the hyperfine structure in the scattering calculations. The paper is organized as follows. Section 2 presents the potential energy surface (PES) used in this work. Details about the treatment for the ND isotopolog is also highlighted. Section 3 describes the scattering formalism for the obtention of both fine- and hyperfine-structure resolved rate coefficients. Fine-structure results are presented and discussed. Then hyperfine resolved rate coefficients are presented. Section 4 presents an illustration of the impact of the new computed rate coefficients in a simple radiative transfer modeling under non-LTE conditions. A summary of the work and our conclusions are presented in Sect. 5.

2. Potential energy surface

In this work we use the four-dimensional PES computed by Pirlot Jankowiak et al. (2021, hereafter Paper I). Ab initio calculations were done for 33 516 geometries with the explicitly

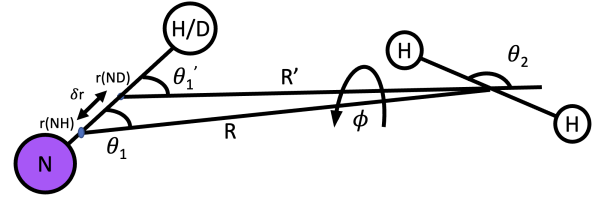


Fig. 1. Description of the NH- H_2 and ND- H_2 complexes in Jacobi coordinates. Unprimed and primed coordinates relate to NH and ND, respectively.

correlated coupled cluster single, double, and a perturbative treatment of triple excitations [RCCSD(T)-F12a] (Knizia et al. 2009) using the MOLPRO software (Werner et al. 2020). The augmented correlation-consistent polarized valence triple zeta (aug-cc-pVTZ) basis set (Dunning 1989) was used and the counterpoise scheme of Boys & Bernardi (1970) was considered to take into account the basis set superposition error.

This PES is provided as a function of the Jacobi coordinate system. The origin of this coordinate system lies at the center of mass of NH, with the intermolecular separation between NH and H_2 centers of mass denoted as the vector \mathbf{R} , aligned along the z -axis. The rotational motion of NH around the R axis is described by the angle θ_1 , while the angles (θ_2, ϕ) specify the orientation of H_2 (see Fig. 1).

In this PES, both NH and H_2 are treated as rigid rotors. We consider the internuclear distances taken in the average of the vibrational ground state for both species, with $r_{\text{NH}} = 1.958a_0$ and $r_{\text{HH}} = 1.449a_0$ (Huber & Herzberg 1979).

To make this PES suitable for time-independent quantum scattering calculations, the analytical representation of the potential was done in terms of bispherical harmonics, given by

$$V(R, \theta_1, \theta_2, \phi) = \sum_{l_1 l_2 l} v_{l_1 l_2 l}(R) A(\theta_1, \theta_2, \phi) \quad (1)$$

$$A(\theta_1, \theta_2, \phi) = \sqrt{\frac{2l+1}{4\pi}} \left[\begin{pmatrix} l_1 & l_2 & l \\ 0 & 0 & 0 \end{pmatrix} P_{l_1 0}(\theta_1) P_{l_2 0}(\theta_2) \right. \\ \left. + 2 \sum_{m=1}^{\min(l_1, l_2)} \begin{pmatrix} l_1 & l_2 & l \\ m & -m & 0 \end{pmatrix} \right. \\ \left. \times P_{l_1 m}(\theta_1) P_{l_2 m}(\theta_2) \cos(m\phi) \right]. \quad (2)$$

Here P_{lm} denotes associated Legendre polynomials, and (\dots) represents 3j-Wigner symbols; l_1, l_2 , and l are defined such that $|l_1 - l_2| < l < l_1 + l_2$. Then, the expansion coefficients $v_{l_1 l_2 l}(R)$ are determined through a least-squares fitting procedure, setting $l_1^{\text{max}} = 10$ and $l_2^{\text{max}} = 4$ and resulting in a total of 86 terms for subsequent scattering calculations.

The global minimum was found to be $D_e = 149.10 \text{ cm}^{-1}$ corresponding to a linear geometry characterized by $R = 6.30a_0$, $\theta_1 = 180^\circ$, $\theta_2 = 0^\circ$, and $\phi = 0^\circ$, where one hydrogen atom is oriented toward the nitrogen end. Additionally, a secondary minimum was observed for a T-shaped geometry with $R = 6.77a_0$, $\theta_1 = 0^\circ$, $\theta_2 = 90^\circ$, and $\phi = 0^\circ$, exhibiting a well depth $D_e = 109.52 \text{ cm}^{-1}$. This PES has undergone validation, displaying good agreement between bound state calculations and experimental measurements from Fawzy et al. (2005).

The deuteration of NH yields the ND molecule by a displacement of the center of mass of $\delta r = -0.1149a_0$ toward the

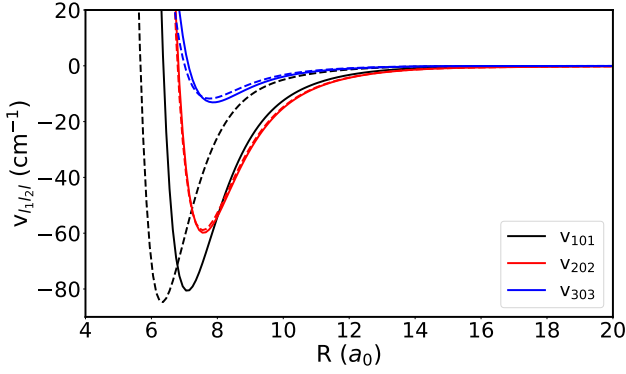


Fig. 2. First expansion coefficients $v_{l_1 l_2 l}(R)$ for the NH–H₂ (solid) and ND–H₂ (dashed) collisional systems.

deuterium end. To assess the interaction potential for the ND–H₂ complex, we introduce new coordinates (R' , θ'_1) and transform the primary isotopolog coordinates as follows:

$$R' = \sqrt{R^2 + \delta r^2 + 2R\delta r \cos(\theta_1)}, \quad (3)$$

$$\theta'_1 = \cos^{-1} \left(\frac{R \cos(\theta_1) - \delta r}{R'} \right). \quad (4)$$

Within the rigid rotor approximation, we assume that the bond lengths for NH and ND remain identical. Notably, we found that the transformation of the (θ_2 , ϕ) angles have no impact on the dynamics calculations and was not necessary. In order to obtain an analytical representation suitable for scattering calculations, a Gauss-Legendre quadrature procedure was performed for 588 geometries from the transformed NH–H₂ PES with $l_1^{\max} = 10$ and $l_2^{\max} = 4$.

Figure 2 displays the first radial coefficients $v_{l_1 l_2 l}(R)$ for both NH–H₂ and ND–H₂ complexes. The most significant difference arises from the v_{101} term. This term exhibits a lower magnitude for the ND–H₂ PES than the NH–H₂ PES, indicating a more pronounced odd anisotropy for the NH–H₂ complex. This effect was already seen for the NH/ND–He collisional systems in the study of Dumouchel et al. (2012). We anticipate that the incorporation of these radial coefficients in scattering calculations will lead to differences in cross sections between the two isotopologs.

3. Scattering calculations

3.1. Fine-structure excitation

The NH and ND radicals are both open-shell molecules, and possess a nonzero electronic spin $S = 1$. This is coupled to the spin-free rotational angular momentum n_1 such that

$$\mathbf{j}_1 = \mathbf{n}_1 + \mathbf{S},$$

where j_1 is the total rotational angular momentum of the target. Then, in the $^3\Sigma^-$ ground electronic state, the NH and ND rotational levels are split by spin-rotation and spin-spin interaction. In the intermediate coupling scheme, the wave function can be defined for $j_1 \geq 1$ as (Gordy & Cook 1984)

$$\begin{aligned} |F_1 j_1 m\rangle &= \cos(\alpha) |j_1 - S, j_1 m\rangle + \sin(\alpha) |j_1 + S, j_1 m\rangle \\ |F_2 j_1 m\rangle &= |j_1, j_1 m\rangle \\ |F_3 j_1 m\rangle &= -\sin(\alpha) |j_1 - S, j_1 m\rangle + \cos(\alpha) |j_1 + S, j_1 m\rangle \end{aligned} \quad (5)$$

Table 1. Spectroscopic constants of NH and ND radicals in their $^3\Sigma^-$ electronic state.

Parameters ^(a)	NH ^(b)	ND ^(c)
B_0	16.343	8.782
D_0	1.703×10^{-4}	4.880×10^{-4}
γ_0	-5.485×10^{-2}	-2.947×10^{-2}
λ_0	0.920	0.919
μ_D	1.39 ^(d)	1.39

Notes. ^(a)The values of the parameters are given in cm^{-1} . ^(b)Flores-Mijangos et al. (2004). ^(c)Takano et al. (1998). ^(d)The value of μ_D is given in Debye (Keun Park & Sun 1993).

where $|n_1, j_1 m\rangle$ denotes the wave function in a pure Hund's case (b), and α is the angle arising from the diagonalization of the molecular Hamiltonian. In the pure Hund's case (b) limit ($\alpha \rightarrow 0$), the F_i labels are associated with $n_1 = j_1 - S$ for F_1 and $n_1 = j_1 + S$ for F_3 . For simplicity, fine-structure levels are labeled as n_{1, j_1} corresponding to the pure Hund's case (b) limit, although all calculations were done in the intermediate coupling scheme. In the CC approach, the NH or ND angular momentum couples with the rotational angular momentum j_2 of the H₂ collider to form the resultant sum j_{12} . This couples to the orbital angular momentum L to yield the total angular momentum J :

$$\mathbf{j}_{12} = \mathbf{j}_1 + \mathbf{j}_2 \quad \mathbf{J} = \mathbf{j}_{12} + \mathbf{L}.$$

This is the general approach used to compute fine-structure resolved cross sections with the CC procedure.

By the resolution of the CC equations, it is possible to determine fine-structure state-to-state cross sections defined as

$$\sigma_{n_1 j_1 j_2 \rightarrow n'_1 j'_1 j'_2}^{\text{CC}} = \frac{\pi}{k_{n_1 j_1 j_2}^2 [j_1] [j_2]} \sum_{JLL} [J] |T_{n_1 j_1 j_2 j_2 L, n'_1 j'_1 j'_2 j'_2 L'}^J|^2, \quad (6)$$

where $k_{n_1 j_1 j_2}^2$ is the wave vector of the initial state, $[X] \equiv (2X + 1)$ and $T_{n_1 j_1 j_2 j_2 L, n'_1 j'_1 j'_2 j'_2 L'}^J$ are the T -matrix elements (i.e., the solutions of the CC equations). The rate coefficient from an initial state ($n_1 j_1 j_2$) to a final state ($n'_1 j'_1 j'_2$) can be obtained by integrating the CC cross section in Eq. (6) over a Maxwell-Boltzmann distribution of the collisional energy E_c :

$$\begin{aligned} k_{n_1 j_1 j_2 \rightarrow n'_1 j'_1 j'_2}^{\text{CC}}(T) &= \left(\frac{8}{\pi \mu (k_B T)^3} \right)^{1/2} \\ &\times \int_0^\infty \sigma_{n_1 j_1 j_2 \rightarrow n'_1 j'_1 j'_2}^{\text{CC}}(E_c) E_c e^{-E_c/k_B T} dE_c \end{aligned} \quad (7)$$

with μ the reduced mass of the collisional system and k_B the Boltzmann constant.

Details of the scattering calculations can be found in Appendix A. The spectroscopic parameters used in fine-structure calculations for NH and ND are summarized in Table 1. The scattering calculations were done using the HIBRIDON package of programs (Alexander et al. 2023).

3.2. Results

Figures 3 and 4 illustrate the temperature dependence of the fine-structure resolved rate coefficients for NH and ND in collision with ortho- and para-H₂. The magnitude of the rate coefficients

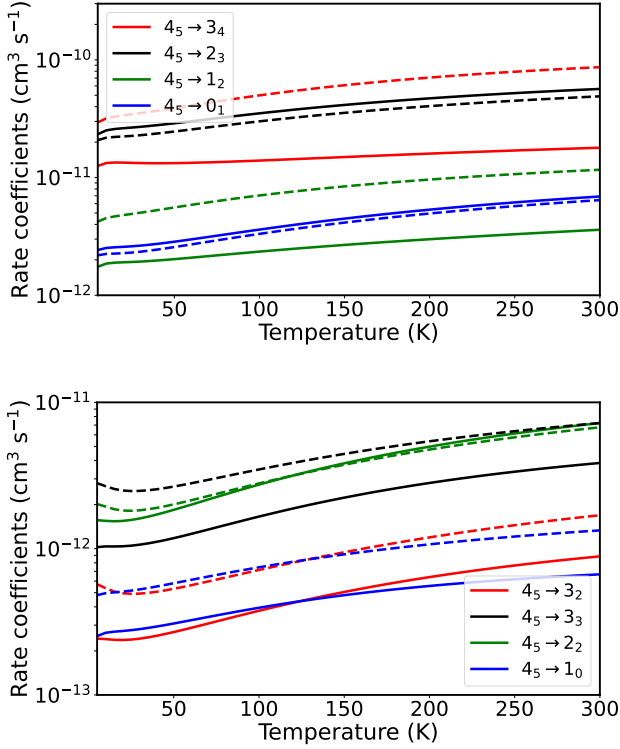


Fig. 3. Temperature dependence of fine-structure resolved de-excitation rate coefficients for NH in collision with para-H₂ (solid) and ortho-H₂ (dashed). The fine-structure conserving transitions ($\Delta n_1 = \Delta j_1$) are presented in the top panel; the fine-structure changing transitions ($\Delta n_1 \neq \Delta j_1$) are shown in the bottom panel.

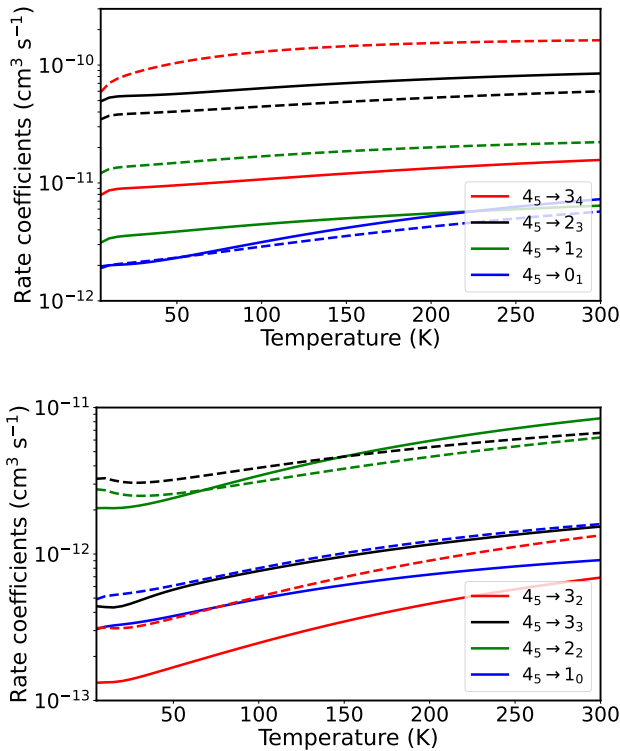


Fig. 4. Temperature dependence of fine-structure resolved de-excitation rate coefficients for ND in collision with para-H₂ (solid) and ortho-H₂ (dashed). The fine-structure conserving transitions ($\Delta n_1 = \Delta j_1$) are presented in the top panel; the fine-structure changing transitions ($\Delta n_1 \neq \Delta j_1$) are shown in the bottom panel.

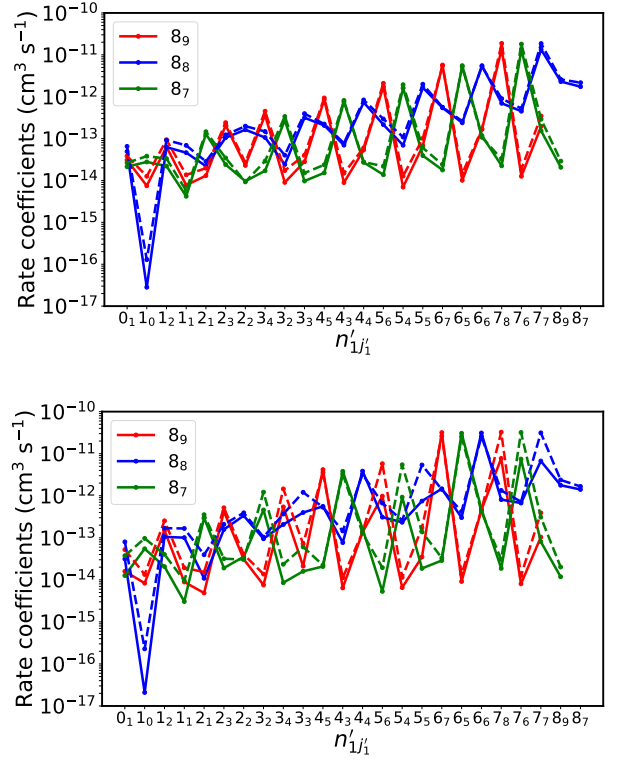


Fig. 5. Fine-structure resolved rate coefficients at 50 K for NH (top) and ND (bottom) de-excitations out of the $n_{1,j_1} = 8_{j_1}$ rotational level.

can vary up to a factor of 3 between low and high temperatures. In addition, most of the rate coefficients for transitions induced by ortho-H₂ are larger than those induced by para-H₂ by a factor of 3–10. This behavior arises due to the contributions of radial coefficients $v_{l_1 l_2 l}$ to the coupling between energy levels in scattering calculations. Specifically, ortho-H₂ collisions involve coefficients with $l_2 = 0, 2$, whereas para-H₂ collisions only consider coefficients with $l_2 = 0$. The ortho-H₂ collisions are then characterized by enhanced anisotropy for $j_2 > 0$ in the PES and tend to yield larger rate coefficients than for para-H₂ collisions, a well-known trend in neutral collisional systems involving H₂ (Kalugina & Lique 2015; Desrousseau et al. 2021; Demes et al. 2023).

As previously reported in Paper I, NH–ortho-H₂ collisions exhibit larger rate coefficients for odd Δn_1 transitions compared to NH–para-H₂ collisions. This is related to the magnitude of the v_{121} radial coefficient, which has a greater intensity compared to those with $l_2 = 0$ and provides a larger contribution in the coupling terms of the CC equations. A similar behavior is also observed for collisions involving ND.

Furthermore, Figs. 3 and 4 display that fine-structure conserving transitions ($\Delta n_1 = \Delta j_1$) dominate over fine-structure changing transitions ($\Delta n_1 \neq \Delta j_1$). Alexander & Dagdigan (1983) already investigated this propensity rule. This rule implies that the electronic spin acts as a spectator during collisions, conserving its projection, due to the absence of electronic spin dependence in the potential energy surface. The rule can be seen clearly in Fig. 5.

It is interesting to have a look at the impact of the isotopic substitution on the rate coefficients. Figure 6 compares rate coefficients for NH and ND in collisions with ortho- and para-H₂. The ND transitions exhibit rate coefficients that are nearly three

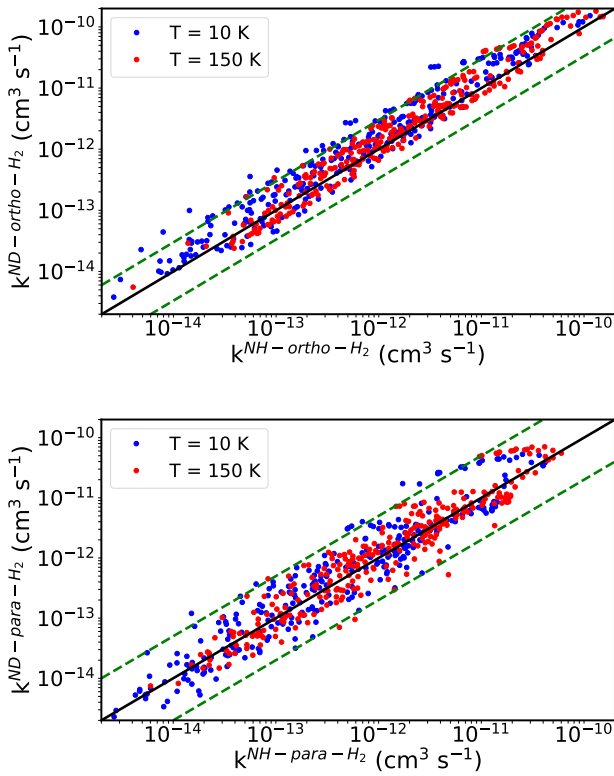


Fig. 6. Systematic comparison between NH and ND rate coefficients at 10 and 150 K. The top panel shows ortho-H₂ collisions, where the green dashed lines quantify deviations by a factor of 3. The bottom panel is related to para-H₂ collisions and the green dashed lines present differences of a factor of 5.

times larger than NH transitions for ortho-H₂ collisions, a disparity that jumps to a factor of 5 for para-H₂ collisions. This discrepancy arises from the displacement of the center of mass between NH-H₂ and ND-H₂ PESs and differences in NH and ND spectroscopic parameters (see Table 1). Similar isotopic differences have been observed in various collisional systems, particularly with light molecules such as NH/ND-He (Dumouchel et al. 2012) and OH/OD-H₂ (Dagdigian 2021). These differences become less pronounced for heavier molecules, as seen in HCO⁺/DCO⁺-H₂ (Denis-Alpizar et al. 2020).

When collisional data involving H₂ are not available, it is customary to use He as a proxy to estimate rate coefficients for the para-H₂(*j*₂ = 0) collider, based on the assumption that their cross sections are similar. Both He and para-H₂(*j*₂ = 0) possess two valence electrons and have a spherical shape. For NH or ND collisions, a mass-scaling relation can be used to model para-H₂ with He

$$k_{X\text{-para-H}_2}(T) \sim \left(\frac{\mu_{X\text{-He}}}{\mu_{X\text{-para-H}_2}} \right)^{1/2} k_{X\text{-He}}(T), \quad (8)$$

where X is either NH or ND.

Figure 7 displays the discrepancies between fine-structure rate coefficients computed in this work with those available from Dumouchel et al. (2012).¹ Specifically, we compare NH and ND

¹ Ramachandran et al. (2018) published more recent data about the NH-He complex that are consistent with those of Dumouchel et al. (2012), but did not provide fine-structure rate coefficients for the ND-He complex.

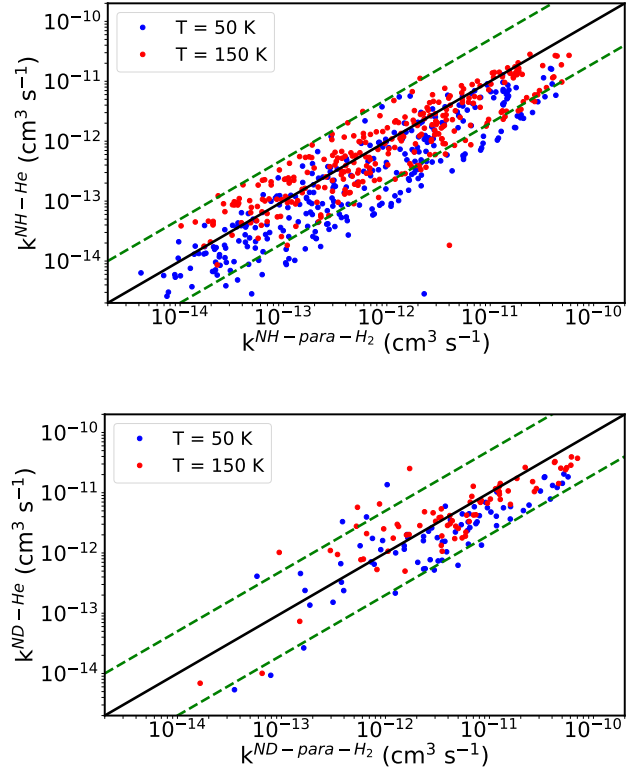


Fig. 7. Comparison between the present fine-structure resolved rate coefficients for NH and ND in collision with para-H₂ and those in collision with He done by Dumouchel et al. (2012). The dashed lines represent deviations of the data of a factor of 5.

in collision with para-H₂ and scaled-He. In the case of NH, substantial differences are observed. The para-H₂ rate coefficients are larger than those of He by more than a factor of 5, particularly at low temperatures (*T* ≤ 50 K). Some transitions can exhibit larger deviations even at higher temperatures, showing a strong temperature-dependence between the datasets. A similar behavior is observed in the case of ND. This could be explained by the contrasts in the interaction potentials. The PES calculated for NH-He by Cybulski et al. (2005) presents a well depth smaller by a factor ~7 compared to the NH-H₂ PES computed in Paper I. This difference leads to larger cross sections for para-H₂ collisions. As a conclusion, He is an unsuitable template for para-H₂(*j*₂ = 0) collisions, necessitating the explicit computation of these rate coefficients.

3.3. Hyperfine-structure excitation

Additional energy splittings occur for NH and ND due to the presence of the nuclear spins of the hydrogen, deuterium, and nitrogen atoms, *I*_H = 1/2, *I*_D = 1, and *I*_N = 1, respectively. These spins couple to the rotational quantum number, as

$$\mathbf{F}_1 = \mathbf{j}_1 + \mathbf{I}_{\text{H/D}} \quad \mathbf{F} = \mathbf{F}_1 + \mathbf{I}_{\text{N}}$$

with *F*₁ and *F* being the rotational quantum numbers including nuclear spins of the targeted isotopolog. Such splittings are generally small (10⁻³–10⁻⁴ cm⁻¹) due to the magnitude of the possible electric quadrupole and magnetic moments. In the case of NH, each rotational level (*n*₁ > 2) possesses 18 hyperfine components except for *n*₁ = 0, 1, 2, which have respectively 5, 13, and 17 hyperfine energy levels. For ND these splittings lead to 27 levels for *n*₁ > 2 and 7, 19, and 26 levels for *n*₁ = 0, 1, 2.

Collisional excitation between two molecules is a computational challenge, particularly in calculations involving open-shell molecules with two nonzero nuclear spins. The computational cost of scattering calculations becomes prohibitive with our current computational resources, due to the extensive number of channels that must be considered. For NH and ND, our objective is to provide hyperfine rate coefficients up to 200 K, taking into account energy levels up to 326 cm^{-1} for NH and up to 100 K with energy levels up to 176 cm^{-1} for ND. Achieving this goal entails accounting for 71 energy levels in the case of NH and 105 for ND. To account both the nuclear spins of the target and the internal structure of the collider, the IOS limit is tested and used.

3.3.1. Infinite-order sudden limit approach

It is possible to estimate state-to-state hyperfine resolved rate coefficients only by considering the fine-structure rate coefficient ($k_{n_1 j_1 j_2 \rightarrow n'_1 j'_1 j'_2}^{\text{CC}}$) out of the fundamental energy level. Based on several works (Alexander 1982; Orlikowski 1985; Lanza & Lique 2014), the hyperfine resolved rate coefficient for a $^3\Sigma$ electronic state molecule in collision with ortho- and para- H_2 can be written for an initial state $i = (n_1 j_1 F_1 F_j)$ to a final one $f = (n'_1 j'_1 F'_1 F'_j)$ as (see details in Appendix B)

$$k_{i \rightarrow f}^{\text{IOS-p}}(T) = [n_1 n'_1 j_1 j'_1 F_1 F'_1 F_j F'_j] \sum_{\lambda_1, \lambda_2} \frac{[\lambda_1]}{\lambda_1 + 1} \begin{pmatrix} n'_1 & \lambda_1 & n_1 \\ 0 & 0 & 0 \end{pmatrix}^2 \times \begin{pmatrix} j'_2 & \lambda_2 & j_2 \\ 0 & 0 & 0 \end{pmatrix}^2 \left\{ \begin{matrix} n'_1 & n_1 & \lambda_1 \\ j_1 & j'_1 & S \end{matrix} \right\}^2 \times \left\{ \begin{matrix} j_1 & j'_1 & \lambda_1 \\ F'_1 & F_1 & I_X \end{matrix} \right\}^2 \left\{ \begin{matrix} F_1 & F'_1 & \lambda_1 \\ F' & F & I_N \end{matrix} \right\}^2 \times k_{100 \rightarrow \lambda_1 + 1, \lambda_1, \lambda_2}^{\text{CC}}(T) \quad (9)$$

$$k_{i \rightarrow f}^{\text{IOS-o}}(T) = [n_1 n'_1 j_1 j'_1 F_1 F'_1 F_j F'_j] \sum_{\lambda_1, \lambda_2} \frac{[\lambda_1]}{\lambda_1 + 1} \frac{[\lambda_2]}{\lambda_2 + 1} \times \begin{pmatrix} n'_1 & \lambda_1 & n_1 \\ 0 & 0 & 0 \end{pmatrix}^2 \begin{pmatrix} j'_2 & \lambda_2 & j_2 \\ 0 & 0 & 0 \end{pmatrix}^2 \left\{ \begin{matrix} n'_1 & n_1 & \lambda_1 \\ j_1 & j'_1 & S \end{matrix} \right\}^2 \times \left\{ \begin{matrix} j_1 & j'_1 & \lambda_1 \\ F'_1 & F_1 & I_X \end{matrix} \right\}^2 \left\{ \begin{matrix} F_1 & F'_1 & \lambda_1 \\ F' & F & I_N \end{matrix} \right\}^2 \times k_{101 \rightarrow \lambda_1 + 1, \lambda_1, \lambda_2 + 1}^{\text{CC}}(T), \quad (10)$$

where $[abc \dots] \equiv (2a+1)(2b+1)(2c+1) \dots$, λ_1, λ_2 are chosen so that $|j_1 - j'_1| \leq \lambda_1 \leq j_1 + j'_1$ and $|j_2 - j'_2| \leq \lambda_2 \leq j_2 + j'_2$, $X \equiv \text{H}$ or D . Moreover, IOS-p stands for collisions with para- H_2 , whereas IOS-o stands for ortho- H_2 collisions. Equations (9) and (10) are used considering NH and ND in a pure Hund's case (b) limit. It should be noted that the rate coefficient can be replaced by the cross section for IOS calculations. Equations (9) and (10) can also be used by considering de-excitations rate coefficients through the detailed balance:

$$k_{100 \rightarrow \lambda_1 + 1, \lambda_1, \lambda_2}^{\text{CC}}(T) = [\lambda_1][\lambda_2] k_{\lambda_1 + 1, \lambda_1, \lambda_2 \rightarrow 100}^{\text{CC}}(T), \quad (11)$$

$$k_{101 \rightarrow \lambda_1 + 1, \lambda_1, \lambda_2 + 1}^{\text{CC}}(T) = \frac{[\lambda_1][\lambda_2 + 1]}{3} k_{\lambda_1 + 1, \lambda_1, \lambda_2 + 1 \rightarrow 101}^{\text{CC}}(T). \quad (12)$$

It is worth noting that the gap between hyperfine energy levels remains relatively small compared to the collisional energies involved. Consequently, it is reasonable to anticipate that the

IOS limit can provide reliable predictions for hyperfine resolved transitions. Then, the scaling relation can be used, first introduced by Neufeld & Green (1994, hereafter NG) as

$$k_{n_1 j_1 F_1 F_j \rightarrow n'_1 j'_1 F'_1 F'_j}^{\text{NG}}(T) = \frac{k_{n_1 j_1 F_1 F_j \rightarrow n'_1 j'_1 F'_1 F'_j}^{\text{IOS}}(T)}{k_{n_1 j_1 j_2 \rightarrow n'_1 j'_1 j'_2}^{\text{IOS}}(T)} k_{n_1 j_1 j_2 \rightarrow n'_1 j'_1 j'_2}^{\text{CC}}(T). \quad (13)$$

This relation is constructed so that the summation of the rate coefficients over the final hyperfine labels for a given transition gives the CC fine-structure rate coefficient:

$$\sum_{F'_1 F'_j} k_{n_1 j_1 F_1 F_j \rightarrow n'_1 j'_1 F'_1 F'_j}^{\text{NG}}(T) = k_{n_1 j_1 j_2 \rightarrow n'_1 j'_1 j'_2}^{\text{CC}}(T). \quad (14)$$

One can see that using Eq. (13) implies that the calculation of quasi-elastic transitions (i.e., $n_1 = n'_1$, $j_1 = j'_1$ and with $F_1 \neq F'_1$ and $F \neq F'$) requires the determination of fine-structure elastic transitions. However, these transitions are usually difficult to converge. In the following we provide quasi-elastic transitions without the NG correction and only using the IOS limit through Eqs. (9) and (10). In addition, the presence of 3j and 6j Wigner coefficients involves strict propensity rules. In particular, the 3j coefficient sets all hyperfine rate coefficients to zero for the case where $n_1 = n'_1 = 0$. The corresponding rate coefficients are only nonvanishing for hyperfine elastic transitions, which are beyond the scope of this work.

3.3.2. Validation of the IOS approach

The IOS approximation described previously can be tested and compared with the recoupling approach. This reference method, for hyperfine treatment can be found in detail in Alexander & Dagdigian (1985), among others. This comparison is applied to the NH- H_2 and ND- H_2 collisional systems, but taking into account only the nuclear spin of the hydrogen (or the deuterium). The IOS approach was tested for several cross sections at two different collisional energies.

Figure 8 displays a comparison of cross sections computed using the NG correction and the recoupling approach for NH and ND in collision with both ortho- and para- H_2 . Quasi-elastic transitions, calculated with the IOS approximation, are also included in these plots. Of all the tested collisional systems, the figure shows that most of the largest transitions match almost perfectly those obtained with the recoupling approach. It is possible to quantify the discrepancies between methods by introducing the weighted mean error factor (WMEF; Loreau et al. 2018),

$$\text{WMEF} = \frac{\sum_{i \rightarrow f} \sigma_{i \rightarrow f}^{\text{rec}} r_i}{\sum_i \sigma_{i \rightarrow f}^{\text{rec}}}, \quad (15)$$

with $\sigma_{i \rightarrow f}^{\text{rec}}$ being the hyperfine cross section obtained with the recoupling approach, $r_i = \max(\sigma_{i \rightarrow f}^{\text{rec}} / \sigma_{i \rightarrow f}^{\text{NG}}, \sigma_{i \rightarrow f}^{\text{NG}} / \sigma_{i \rightarrow f}^{\text{rec}})$. Larger discrepancies are observed for low collisional energies, while most transitions exhibit better agreement at higher energies. For para- H_2 collisions, the WMEFs remain of the same order of magnitude for NH and ND, regardless of the energy. The inclusion of quasi-elastic transitions has minimal impact in this case. Among all the tested collisional systems, ortho- H_2 collisions display the most noticeable deviations, mostly due to the inclusion of quasi-elastic transitions, which are among the most divergent transitions in terms of intensity. However, it is interesting to note that, with the exception of these transitions, the NG correction performs surprisingly well in the case of ortho- H_2 collisions.

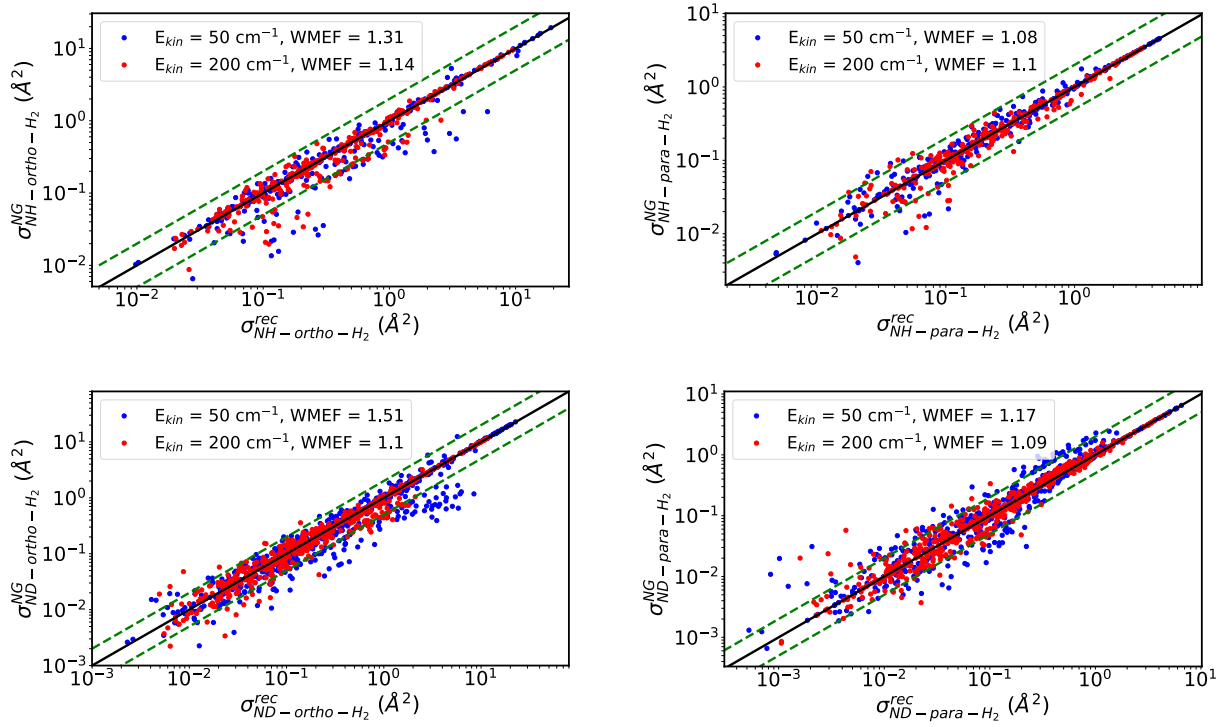


Fig. 8. Comparison between the NG correction and the recoupling approach for NH (top) and ND (bottom) cross sections for collisions with ortho- (left) and para-H₂ (right). Cross sections are displayed for collisional energies of 50 and 200 cm⁻¹. Quasi-elastic transitions computed in the IOS limit are also present. The dashed lines represent deviations of the data of a factor of 2.

3.3.3. NH–H₂ and ND–H₂ rate coefficients

Figure 9 displays the propensity rules discussed in Sect. 3.1 and applied here to the hyperfine rate coefficients computed through the IOS approach using Eqs. (9), (10), and (13). Among all collisional systems, the strong propensity rule governing $\Delta n_1 = \Delta j_1 = \Delta F_1 = \Delta F$ transitions is found. This rule can be explained by vector coupling arguments. Given the independence of nuclear spins from the potential, they remain spectators during the collision, and they cannot be reoriented. As in Sect. 3.1, ortho-H₂ collisions are governed by the odd Δn_1 propensity rule, except for NH for $\Delta F_1 \neq \Delta F$ transitions, where this rule stands for para-H₂ collisions. These trends are well known for various types of systems having one or two nuclear spins (Daniel et al. 2004; Dumouchel et al. 2012; Kalugina & Lique 2015; Lique et al. 2016; Kłos et al. 2020; Lara-Moreno et al. 2021; Ndaw et al. 2021; Godard Palluet & Lique 2024).

4. Rotational excitation of NH in the ISM

Detections of several NH fine-structure lines in the ejecta of the massive binary star η Carinae have been reported by Gull et al. (2020). Additionally, Goicoechea & Roncero (2022) detected the submillimeter $1_2 \rightarrow 0_1$ fine-structure line in the Orion Bar PDR. To our knowledge, these are the only two sources where NH rotational lines are observed in emission, while all other previous detections report absorption lines. In both studies, modeling based on accurate NH–H₂ collisional data was not possible because of the lack of these data. In the absence of rate coefficients for NH–H₂ collisions, astrophysical modeling relied on He collisional data using the scaling relation given by Eq. (8) or based on crude estimation when even these data are missing.

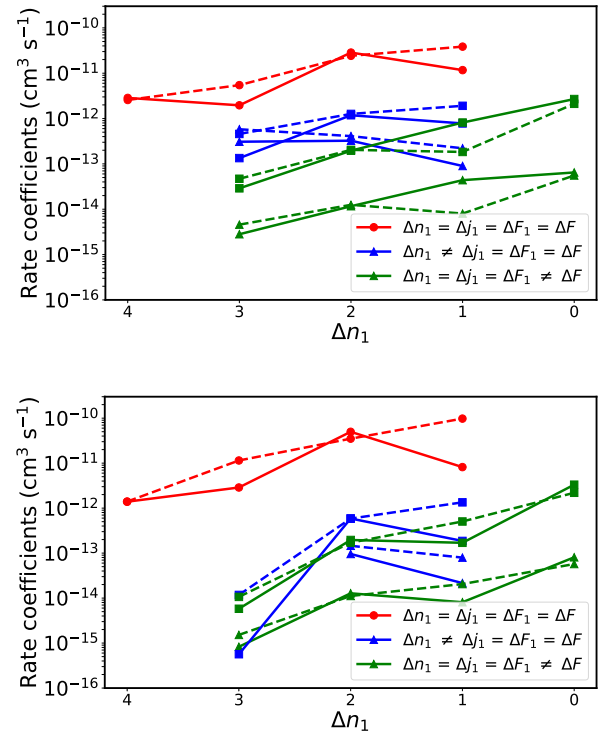


Fig. 9. Hyperfine rate coefficients of NH (top) out of the ($n_1 = 4, j_1 = 5, F_1 = 5.5, F = 6.5$) level and ND (bottom) out of the ($n_1 = 4, j_1 = 5, F_1 = 5, F = 6$) level at 50 K as a function of the variation in the rotational angular momentum n_1 . The solid lines stand for para-H₂ collisions and the dashed lines for ortho-H₂ collisions. The $\Delta F_1 = \Delta F - 2$ and $\Delta n_1 = \Delta j_1 - 2$ transitions are represented by triangles, whereas the $\Delta F_1 = \Delta F - 1$ and $\Delta n_1 = \Delta j_1 - 1$ transitions are represented by squares.

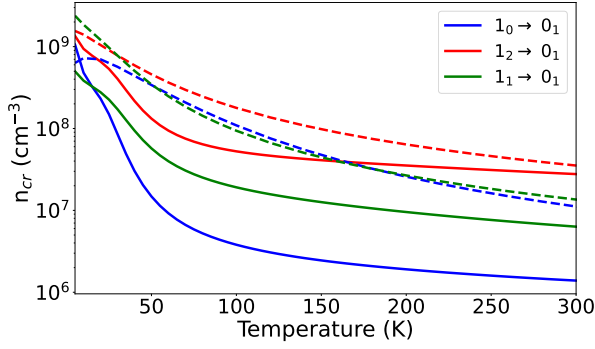


Fig. 10. Evolution of the critical density of NH with the temperature for the fine-structure components of the $1 \rightarrow 0$ line. The solid lines stand for NH–H₂ rate coefficients, whereas the dashed lines stand for NH–He coefficients.

In the following discussions, we focus on the three fine-structure lines $1_0 \rightarrow 0_1$ (946 GHz), $1_2 \rightarrow 0_1$ (974 GHz) and $1_1 \rightarrow 0_1$ (1000 GHz) detected by the *Herschel*/SPIRE survey in the study of Gull et al. (2020) and later toward the Orion Bar PDR with the *Herschel*/HIFI spectrometer by Goicoechea & Roncero (2022). We carried out simple radiative transfer modeling to assess the impact of the new NH–H₂ rate coefficients in comparison to scaled NH–He data. We explored the impact of the new NH–H₂ rate coefficients in modeling for typical conditions of these two environments with the RADEX non-LTE radiative transfer model using the escape probability approximation (Van der Tak et al. 2007).

4.1. General features: Critical densities and background continuum

A useful parameter for qualitatively understanding the excitation behavior of molecular lines is the critical density $n_{\text{cr}}^{ul}(T)$ from an upper level u to a lower one l , describing the gas density where radiative and collisional processes are in competition. Using the new fine-structure NH–H₂ rate coefficients, we estimated these critical densities to be

$$\begin{aligned} n_{\text{cr}}^{ul}(T) &= \frac{\sum_{i<u} A_{ui}}{\sum_{u\neq i} k_{ui}(T)} \\ &= \frac{\sum_{i<u} A_{ui}}{\sum_{u\neq i} \left[\frac{\text{OPR}}{1+\text{OPR}} k_{ui}^{\text{ortho-H}_2}(T) + \frac{1}{1+\text{OPR}} k_{ui}^{\text{para-H}_2}(T) \right]}, \end{aligned} \quad (16)$$

where OPR is the ortho-to-para-H₂ ratio assuming a thermalized distribution of the rotational population of H₂. We note, however, that the OPR can be out of equilibrium in various astrophysical environments, and can reach $\sim 10^{-3}$ at low temperatures (Faure et al. 2019). The A_{ul} are the fine-structure computed Einstein coefficients for NH radiative transitions (see Appendix C). These critical densities are compared to those computed with NH–He rate coefficients, also using Eq. (16), excluding the ortho-H₂ term and the OPR.

Figure 10 displays the critical density n_{cr} for each fine-structure component of the $1 \rightarrow 0$ rotational line. Due to the high rotational constant of NH, Einstein coefficients corresponding to these lines are large, of the order of $A_{ul} \sim 10^{-3} - 10^{-2} \text{ s}^{-1}$. This is why the computed critical densities are high compared to the density of molecular clouds ($n(\text{H}_2) \sim 10^3 - 10^6 \text{ cm}^{-3}$). At very low temperature, a very high gas density is needed to reach the LTE regime. In this case, most of the excitation is due to

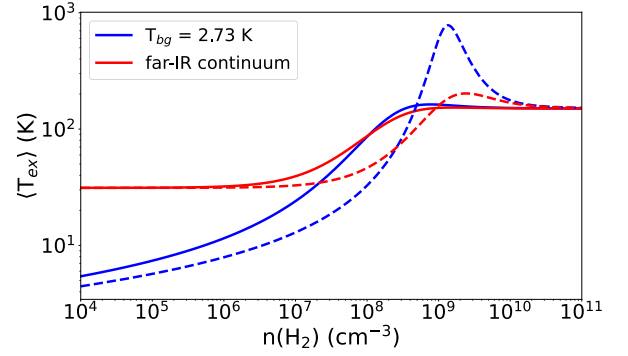


Fig. 11. Dependence of the excitation temperature of the $1 \rightarrow 0$ rotational line on the gas density. The solid lines stand for NH–H₂ rate coefficients, whereas the dashed lines stand for NH–He coefficients.

radiative processes (i.e., when inelastic collisions do not dominate) and NH can be easily detected in absorption toward strong submillimeter continuum sources. It can be seen from Eq. (16) that the evolution of the critical density strongly depends on the OPR, reflecting the importance of collisions induced by ortho-H₂ at high temperatures because of their different excitation efficiency. Discrepancies between H₂ and He critical densities are significant, exceeding an order of magnitude especially for the $1_0 \rightarrow 0_1$ line. These variations persist, even at low temperatures when para-H₂ collisions are dominant, reflecting the previously discussed differences between para-H₂ and He rate coefficients shown in Fig. 7.

It is interesting to assess the impact of rate coefficients on non-LTE modeling using He or H₂ sets of collisional data, particularly in environments influenced by a strong far-IR and submillimeter continuum. As an illustrative example, in these first models we adopt the physical parameters of Gull et al. (2020) for η Carinae; that is, we include a fixed column density $N(\text{NH}) = 5 \times 10^{15} \text{ cm}^{-2}$. We adopt a line width of 188 km/s in the ejecta (see Gull et al. 2020). These broad line widths ensure NH optically thin line emission. The kinetic temperature was chosen to be $T_{\text{k}} = 150 \text{ K}$.

Figure 11 presents the variations in the excitation temperatures derived from models using NH–H₂ and NH–He rate coefficients. We considered two distinct continua: the cosmic microwave background (CMB) described by a single blackbody at $T_{\text{bg}} = 2.73 \text{ K}$ and the modified source continuum that Gull et al. (2020) adopted. We found that excitation temperatures for individual fine-structure lines did not exhibit significant relative differences. Then we computed an average excitation temperature $\langle T_{\text{ex}} \rangle (n_1 = 1 \rightarrow n'_1 = 0)$ over these lines. Radiative processes dominate for very low gas densities, with $\langle T_{\text{ex}} \rangle \approx T_{\text{bg}}$ (i.e., radiative thermalization). Conversely, $\langle T_{\text{ex}} \rangle$ thermalizes to T_{k} when collisional processes are dominant for high densities. Given the typical conditions in η Carinae, a non-LTE behavior is obvious for both continua and sets of collisional data. The influence of the background continuum on excitation temperature is especially pronounced for low densities. When we adopt the specific source continuum, the averaged excitation temperature computed with NH–H₂ rate coefficients depart from a radiative regime at $n(\text{H}_2) \sim 10^7 \text{ cm}^{-3}$, whereas when the continuum is only the CMB, the NH excitation is in the non-LTE regime for a gas density of $\sim 10^4 - 10^5 \text{ cm}^{-3}$. However, the impact of the continuum on the excitation temperature using H₂ rate coefficients is negligible for $n(\text{H}_2) \geq 10^8 \text{ cm}^{-3}$ and excitation temperatures become identical between the two continua. On the other hand,

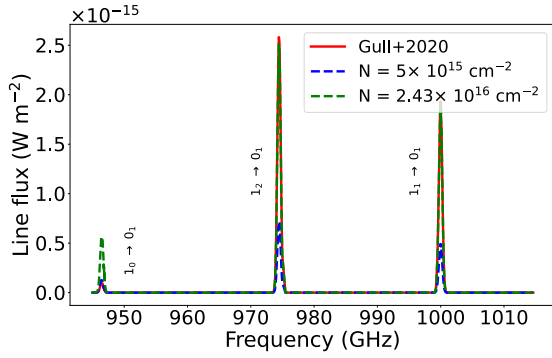


Fig. 12. Models of the NH $1 \rightarrow 0$ rotational line toward η Carinae. The solid curve represents the observations of Gull et al. (2020), while the dashed curves refer to modeling using fine-structure NH–H₂ rate coefficients.

for $n(\text{H}_2) \sim 4 \times 10^8 - 10^{10} \text{ cm}^{-3}$, models computed using the CMB and NH–He rate coefficients predict a supra-thermal excitation ($\langle T_{\text{ex}} \rangle > T_{\text{k}}$) which becomes moderate when we adopt the source continuum. This difference in behavior with the H₂ collisional data is related to the lower magnitude of He rate coefficients. Consequently, excitation temperatures computed from He rate coefficients are more influenced by the strength of the source continuum than those computed using H₂ rate coefficients.

Since the same excitation trends apply for both NH and ND, these results imply that the ND column densities inferred by Bacmann et al. (2016) in the prestellar core 16293E may be revised. Since ND is observed there in emission, a decrease in its calculated abundance can be anticipated. In addition, due to the larger values of the NH–H₂ rate coefficients compared to the NH–He values used in their work, models using the new collisional data may not be as sensitive to the modification of the background source continuum as they suggested.

4.2. Applications to the binary star η Carinae and the Orion Bar PDR

An essential parameter is the column density of the molecules, which allows us to infer the fractional abundance of a given molecule. For the η Carinae ejecta, Gull et al. (2020) determined a column density of $N(\text{NH}) = 5 \times 10^{15} \text{ cm}^{-2}$ for a gas density of $n(\text{H}_2) = 10^8 \text{ cm}^{-3}$ and a kinetic temperature $T_{\text{k}} = 200 \text{ K}$. Using the new set of fine-structure rate coefficients, we investigate the differences between the column density determined in their work and the value estimated in this study.

Figure 12 displays a simple model of the $1 \rightarrow 0$ rotational line compared to the model determined by Gull et al. (2020). Line fluxes computed using the previously determined column density and the new set of fine-structure rate coefficients show a significant deviation from the observations. These differences are likely to be produced by an overestimation of the inelastic rate coefficients by these authors. By fixing the kinetic temperature to $T_{\text{k}} = 200 \text{ K}$ and a gas density to $n(\text{H}_2) = 10^8 \text{ cm}^{-3}$, it is possible to set the column density by minimizing the χ^2 parameter. Based on our new collisional data, the minimization of this parameter must give an estimation of the integrated lines that best reproduce the observations. We found a column density of $N(\text{NH}) = 2.43 \times 10^{16} \text{ cm}^{-2}$, increasing the previous estimation by a factor of ~ 5 . It looks like the two most intense lines are actually able to reproduce much better the observations than the $1_0 \rightarrow 0_1$ line. This may be due to the larger intensity uncertainty of this

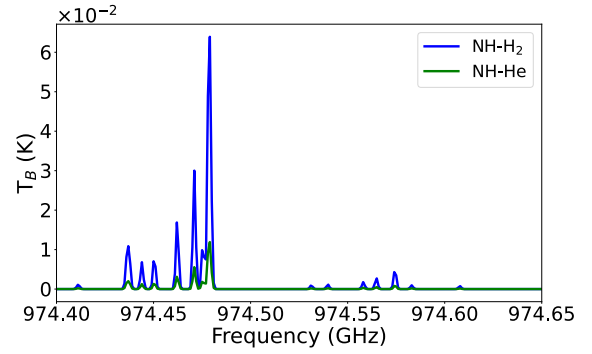


Fig. 13. Model of the NH hyperfine components of the $1_2 \rightarrow 0_1$ line. A line width value of $\Delta v = 0.5 \text{ km s}^{-1}$ is used to avoid overlap of the hyperfine lines displayed in the spectrum. The column density is set to $N(\text{NH}) = 10^{13} \text{ cm}^{-2}$.

weak line or due to anomalous hyperfine emission produced by hyperfine-structure line overlap effects not treated by RADEX.

A 3σ detection of the $1_2 \rightarrow 0_1$ (974 GHz) line in emission toward the Orion Bar was recently reported by Goicoechea & Roncero (2022). These authors estimated the NH excitation conditions and NH column density using a Monte Carlo non-LTE radiative transfer model. For these calculations, the authors used the available fine-structure NH–He collisional data from Toboła et al. (2011) to estimate the NH–H₂ rate coefficients through Eq. (8). These rate coefficients were also extrapolated to high temperatures. They estimated an excitation temperature of 10–15 K for the 974 GHz line and a column density of $1.3 \times 10^{13} \text{ cm}^{-2}$.

Figure 13 shows an illustration of the brightness temperatures for hyperfine transitions corresponding to the $1_2 \rightarrow 0_1$ line. These models were carried out using the new sets of hyperfine resolved rate coefficients, assuming a kinetic temperature of $T_{\text{k}} = 150 \text{ K}$, a gas density $n(\text{H}_2) = 10^5 \text{ cm}^{-3}$, and a typical column density of $N(\text{NH}) = 10^{13} \text{ cm}^{-2}$. The CMB was used as the background continuum and the hyperfine Einstein coefficients were extracted from the CDMS database (Endres et al. 2016). For the different sets of rate coefficients, we found quite important disparities in brightness temperatures. In particular, all the hyperfine-structure line peaks are brighter by a factor of 5 when using H₂ collisional data compared to those obtained with He rate coefficients. It was found that matching brightness temperatures for all components between the two sets of collisional data implied a decrease in the column density by a factor of ~ 5 when using NH–H₂ rate coefficients, leading to $N(\text{NH}) \sim 2 \times 10^{12} \text{ cm}^{-2}$. This discrepancy in column densities is due to the high contribution of ortho-H₂ rate coefficients. At $T_{\text{k}} = 150 \text{ K}$, the thermalized OPR is ~ 2.51 . Then each rate coefficient contributes $0.71 \times k_{ul}^{\text{ortho-H}_2} + 0.29 \times k_{ul}^{\text{para-H}_2}$ to the radiative transfer. As mentioned in the previous sections, the NH–ortho-H₂ rate coefficients are larger than those for NH–para-H₂ by a factor of more than 3, while the NH–para-H₂ rates, being larger than NH–scaled-He rates, are larger by up to a factor of 5.

5. Conclusion

We computed the first fine and hyperfine resolved rate coefficients for NH and ND in collision with both ortho- and para-H₂. These data are based on the 4D PES reported in Paper I. Fine-structure rate coefficients were determined with the CC method up to 300 K, taking into account NH and ND energy levels up to $n_1 = 8$. Both NH and ND displayed significantly larger fine-structure transitions when interacting with ortho-H₂ than with

para-H₂. This trend is standard for light neutral collisional systems. Moreover, these transitions display the usual properties of ³Σ systems where the magnitude of the transitions varies with the transferred angular momentum as ($\Delta n_1 = \Delta j_1$) > ($\Delta n_1 \neq \Delta j_1$).

ND collisions with H₂ yield rate coefficients that differ by a factor of 3–5 with respect to those of NH. These large differences could have been anticipated for such light collisional systems due to the large differences in spectroscopic parameters and the large displacement of the center of mass. Consequently, these findings highlight the importance of computing rate coefficients explicitly for deuterated isotopologs. Additionally, a comparison between H₂ and scaled-He colliders has shown deviations of a factor >5, emphasizing the inadvisability of using of He as a proxy for rate coefficients involving H₂.

The treatment of the hyperfine structure was done using the IOS approach (Faure & Lique 2012) with the NG correction (Neufeld & Green 1994), adapted for the first time to collisions between an open-shell target in a ³Σ electronic state and a linear molecule. This allowed us to provide hyperfine collisional data up to 200 K for NH collisions and 100 K for ND collisions, including energy levels up to $n_1 = 4$. The computed hyperfine rate coefficients follow a strong propensity for $\Delta n_1 = \Delta j_1 = \Delta F_1 = \Delta F$ transitions. A larger gap is observed between $\Delta n_1 \neq \Delta j_1 = \Delta F_1 = \Delta F$ and $\Delta n_1 = \Delta j_1 = \Delta F_1 \neq \Delta F$ transitions in the case of NH as opposed to ND collisions.

The new sets of NH–H₂ fine and hyperfine resolved rate coefficients were included in a radiative transfer modeling for typical conditions of the ejecta of the η Carinae binary star and the Orion Bar PDR where NH submillimeter lines have been detected in emission. We found important differences between the present column densities and those derived in the literature (up to a factor of ~5). These differences are mainly due to the use of the new NH–H₂ rate coefficients. These results suggest a downward revision of the calculation of the abundance of NH (and possibly ND) in these environments using more robust radiative transfer models. These data are expected to be useful for interpreting observations of these species detected in both cold and warm environments where both ortho- and para-H₂ coexist.

The computed collisional data for the fine and hyperfine structure of NH and ND in collision with both ortho- and para-H₂ will be available on the following data bases: EMAA², BASECOL (Dubernet et al. 2024), and LAMDA (Van der Tak et al. 2020).

Acknowledgements. We acknowledge financial support from the European Research Council (Consolidator Grant COLLEXISM, Grant Agreement No. 811363). We wish to acknowledge the support from the CEA/GENCI (Grand Equipement National de Calcul Intensif) for awarding us access to the TGCC (Très Grand Centre de Calcul) Joliot Curie/IRENE supercomputer within the A0110413001 project. J.R.G. thanks the Spanish MICINN for funding support under grant PID2019-106110GB-I00.

References

- Alexander, M. H. 1982, *J. Chem. Phys.*, **76**, 429
 Alexander, M. H., & Dagdigian, P. J. 1983, *J. Chem. Phys.*, **79**
 Alexander, M. H., & Dagdigian, P. J. 1985, *J. Chem. Phys.*, **83**, 2191
 Alexander, M. H., Dagdigian, P. J., Werner, H. J., et al. 2023, *Comp. Phys. Commun.*, **289**, 108761
 Axner, O., Gustafsson, J., Omenetto, N., & Winefordner, J. D. 2004, *Spectrochim. Acta*, **59**, 1
 Bacmann, A., Lefloch, B., Ceccarelli, C., et al. 2003, *ApJ*, **585**, L55
 Bacmann, A., Caux, E., Hily-Blant, P., Parise, B., & Pagani, L. 2010, *A&A*, **521**, L42
 Bacmann, A., Daniel, F., Ceccarelli, C., et al. 2016, *A&A*, **587**, A26
 Boys, S. F., & Bernardi, S. 1970, *Mol. Phys.*, **19**, 553

² <https://dx.doi.org/10.17178/EMAA>

- Caselli, P., Van der Tak, F. F. S., Ceccarelli, C., & Bacmann, A. 2003, *A&A*, **403**, L37
 Ceccarelli, C., Castets, A., Loinard, L., Caux, E., & Tielens, A. G. G. M. 1998, *A&A*, **338**, L43
 Cernicharo, J., Goicoechea, J. R., & Caux, E. 2000, *ApJ*, **534**, L199
 Corey, G. C., & McCourt, F. R. 1983, *J. Chem. Phys.*, **87**, 2723
 Cybulski, H., Krems, R. V., Sadeghpour, H. R., et al. 2005, *J. Chem. Phys.*, **122**
 Dagdigian, P. J. 2021, *MNRAS*, **505**, 1987
 Daniel, F., Dubernet, M. L., & Meuwly, M. 2004, *J. Chem. Phys.*, **121**, 4540
 Daniel, F., Dubernet, M. L., Meuwly, M., Cernicharo, J., & Pagani, L. 2005, *MNRAS*, **363**, 1083
 Demes, S., Lique, F., Loreau, J., & Faure, A. 2023, *MNRAS*, **524**, 2368
 Denis-Alpizar, O., Stoecklin, T., Dutrey, A., & Guilloteau, S. 2020, *MNRAS*, **497**, 4276
 Desrousseaux, B., Quintas-Sánchez, E. L., Dawes, R., Marinakis, S., & Lique, F. 2021, *J. Chem. Phys.*, **154**, 034304
 Dislaire, V., Hily-Blant, P., Faure, A., et al. 2012, *A&A*, **537**, A20
 Dubernet, M. L., Boursier, C., Denis-Alpizar, O., et al. 2024, *A&A*, **683**, A40
 Dumouchel, F., Klos, J., Tobiola, R., et al. 2012, *J. Chem. Phys.*, **137**, 114306
 Dunning, T. H. 1989, *J. Chem. Phys.*, **90**, 1007
 Endres, C. P., Schlemmer, S., Schilke, P., Stutzki, J., & Müller, H. S. P. 2016, *J. Mol. Spectrosc.*, **327**, 95
 Faure, A., & Lique, F. 2012, *MNRAS*, **425**, 740
 Faure, A., Hily-Blant, P., Rist, C., et al. 2019, *MNRAS*, **487**, 3392
 Fawzy, W. M., Kerenskaya, G., & Heaven, M. C. 2005, *J. Chem. Phys.*, **122**, 144318
 Flores-Mijangos, J., Brown, J. M., Matsushima, F., et al. 2004, *J. Mol. Spectrosc.*, **225**, 189
 Gerin, M., Neufeld, D. A., & Goicoechea, J. R. 2016, *ARA&A*, **54**, 181
 Godard Palluet, A., & Lique, F. 2024, *MNRAS*, **527**, 6702
 Goicoechea, J. R., & Roncero, O. 2022, *A&A*, **664**, A190
 Goicoechea, J. R., Rodriguez-Fernandez, N. J., & Cernicharo, J. 2004, *ApJ*, **600**, 214
 Goicoechea, J. R., Lique, F., & Santa-Maria, M. G. 2022, *A&A*, **658**, A28
 Gordy, W., & Cook, R. L. 1984, *Microwave Molecular Spectra* (New Jersey: John Wiley & Sons, Inc)
 Gull, T. R., Morris, P. W., Black, J. H., et al. 2020, *MNRAS*, **499**, 5269
 Hily-Blant, P., Maret, S., Bacmann, A., et al. 2010, *A&A*, **521**, L52
 Huber, K. P., & Herzberg, G. 1979, *Molecular Spectra And Molecular Structure, IV. Constants Of Diatomic Molecules* (New York: Van Nostrand Reinhold)
 Kalugina, Y., & Lique, F. 2015, *MNRAS*, **446**, 21
 Keun Park, J., & Sun, H. 1993, *Chem. Phys. Lett.*, **211**, 6
 Klos, J., Dagdigian, P. J., Alexander, M. H., Faure, A., & Lique, F. 2020, *MNRAS*, **493**, 3491
 Knizia, G., Adler, T. B., & Werner, H. J. 2009, *J. Chem. Phys.*, **130**, 054104
 Lambert, D. L., & Beer, R. 1972, *ApJ*, **177**, 514
 Lanza, M., & Lique, F. 2014, *J. Chem. Phys.*, **141**, 164321
 Lara-Moreno, M., Stoecklin, T., & Halvick, P. 2021, *MNRAS*, **507**, 4086
 Le Gal, R., Hily-Blant, P., Faure, A., et al. 2014, *A&A*, **562**, A83
 Linsky, J. L., Draine, B. T., Moos, H. W., et al. 2006, *ApJ*, **647**, 1106
 Lique, F., Bulut, N., & Roncero, O. 2016, *MNRAS*, **461**, 4477
 Loreau, J., Lique, F., & Faure, A. 2018, *ApJ*, **853**, L5
 Meyer, D. M., & Roth, K. C. 1991, *ApJ*, **376**, L49
 Ndaw, D., Bop, C. T., Dieye, G., Boye Faye, N. A., & Lique, F. 2021, *MNRAS*, **503**, 5976
 Neufeld, D. A., & Green, S. 1994, *ApJ*, **432**, 158
 Orlikowski, T. 1985, *Mol. Phys.*, **56**, 35
 Persson, C. M., De Luca, M., Mookerjee, B., Olofsson, A. O. H., & Black, J. H. 2012, *A&A*, **543**, A145
 Pirlot Jankowiak, P., Kalugina, Y., Ramachandran, R., et al. 2021, *J. Chem. Phys.*, **155**, 134303
 Pirlot Jankowiak, P., Lique, F., & Dagdigian, P. J. 2023, *MNRAS*, **523**, 3732
 Ramachandran, R., Klos, J., & Lique, F. 2018, *J. Chem. Phys.*, **148**, 084311
 Schmitt, J. L. 1969, *PASP*, **81**, 657
 Sobelman, I. I. 1979, *Atomic Spectra and Radiative Transitions* (New York: Springer-Verlag Berlin Heidelberg New York), 1
 Swings, P., Elvey, C. T., & Babcock, H. W. 1941, *ApJ*, **94**, 320
 Takano, S., Klaus, T., & Winnewisser, G. 1998, *J. Mol. Spectrosc.*, **192**, 309
 Tobiola, R., Dumouchel, F., Klos, J., & Lique, F. 2011, *J. Chem. Phys.*, **134**, 024305
 Van der Tak, F. F. S., Black, J. H., Schöier, F. L., Jansen, D. J., & van Dishoeck, E. F. 2007, *MNRAS*, **468**, 627
 Van der Tak, F. F. S., Lique, F., Faure, A., Black, J. H., & van Dishoeck, E. F. 2020, *Atoms*, **8**, 15
 Wagenblast, R., Williams, D. A., Millar, T. J., & Nejad, L. A. M. 1993, *MNRAS*, **260**, 420
 Werner, H. J., Knowles, P. J., Manby, F. R., et al., F. R. M. 2020, *J. Chem. Phys.*, **152**, 144107

Appendix A: Scattering parameters used for dynamical calculations

The resolution of the CC equations requires optimizing several parameters in order to converge fine-structure cross sections for different total energies E_{tot} . For NH and ND in collision with ortho- and para- H_2 , the total energy grid is chosen with an increasing step ΔE with the energy. The step is small at low energies to be able to describe resonances and becomes larger at higher energies to save computational time since the energy variation of the cross sections become smoother. The converged rotational basis n_{max} of the target considered and the total angular momentum J_{tot} are presented in the Tables A.1–A.2. These parameters were chosen in order to converge integral cross sections to 1% accuracy per parameter. The wavefunctions were propagated for all collisional systems from $3.75a_0$ to $60a_0$. The inclusion of the rotational basis $j_2^{\text{max}} = 0, 2$ for para- H_2 and $j_2^{\text{max}} = 1$ for ortho- H_2 were found to be enough for converged scattering calculations. As reported in Paper I, the impact of higher basis for both colliders on cross sections is less than 5% around $E_{\text{tot}} = 500 \text{ cm}^{-1}$ and can be neglected. The reduced mass used for the NH- H_2 and ND- H_2 collisional systems are respectively 1.777 and 1.790 amu.

Appendix B: Details about IOS scaling relations

We describe here a more detailed derivation of the IOS scaling relations. From Eq. (6), it is possible to use angular momentum algebra in order to write the collisional integral cross section between a $^3\Sigma$ target and a linear collider so that

$$\begin{aligned} \sigma_{n_1 j_1 j_2 \rightarrow n'_1 j'_1 j'_2} &= [n_1 n'_1 j'_1 j'_2] \sum_{\lambda_1 \lambda_2 \lambda} \begin{pmatrix} n'_1 & \lambda_1 & n_1 \\ 0 & 0 & 0 \end{pmatrix}^2 \\ &\times \begin{pmatrix} j'_2 & \lambda_2 & j_2 \\ 0 & 0 & 0 \end{pmatrix}^2 \left\{ \begin{matrix} j_1 & n_1 & S \\ n'_1 & j'_1 & \lambda_1 \end{matrix} \right\}^2 \\ &\times \sigma_{\lambda_1 \lambda_2 \lambda}, \end{aligned} \quad (\text{B.1})$$

where $\sigma_{\lambda_1 \lambda_2 \lambda}$ is a quantity defined as

$$\sigma_{\lambda_1 \lambda_2 \lambda} = \frac{\pi}{k^2} \sum_{LL'} (4\pi)^{-3} [\lambda LL'] \begin{pmatrix} L' & \lambda & L \\ 0 & 0 & 0 \end{pmatrix}^2 T_{\lambda_1 \lambda_2 \lambda}^2 \quad (\text{B.2})$$

and $T_{\lambda_1 \lambda_2 \lambda}$ represents the IOS T -matrix coefficients excluding the angular dependence, similar to the coefficients defined by [Corey & McCourt \(1983\)](#) applied for atom-molecule collisions.

Table A.1. Converged parameters used in close-coupling calculations for the NH- H_2 collisional system.

NH-ortho- H_2				NH-para- H_2			
E_{tot} (cm $^{-1}$)	ΔE (cm $^{-1}$)	n_{max}	J_{tot}	E_{tot} (cm $^{-1}$)	ΔE (cm $^{-1}$)	n_{max}	J_{tot}
150.3–153.7	0.1	7	8	31.6–35.0	0.1	7	15
153.8–168.7	0.1	7	13	35.1–50.0	0.1	7	20
168.8–218.7	0.1	7	20	50.1–100.0	0.1	7	23
218.8–318.7	0.1	10	40	100.1–200.0	0.1	8	28
318.9–418.7	0.2	10	60	200.2–300.0	0.2	10	50
419.2–618.7	0.5	10	70	300.5–500.0	0.5	10	60
619.2–818.7	0.5	10	85	500.5–700.0	0.5	10	65
819.7–1118.7	1	11	90	701–1000	1	12	80
1123.7–1318.7	5	12	95	1005–1200	5	12	85
1323.7–1618.7	5	12	100	1205–1500	5	13	115
1623.7–2118.7	5	14	125	1505–2000	5	13	120
2168.7–2568.7	50	15	140	2050–2450	50	14	125

Table A.2. Converged parameters used in close-coupling calculations for the ND- H_2 collisional system.

ND-ortho- H_2				ND-para- H_2			
E_{tot} (cm $^{-1}$)	ΔE (cm $^{-1}$)	n_{max}	J_{tot}	E_{tot} (cm $^{-1}$)	ΔE (cm $^{-1}$)	n_{max}	J_{tot}
135.2–153.7	0.1	6	15	16.5–35.0	0.1	6	15
153.8–168.7	0.1	6	18	35.1–50.0	0.1	7	17
168.8–218.7	0.1	8	24	50.1–100.0	0.1	8	21
218.8–318.7	0.1	8	33	100.1–200.0	0.1	8	27
318.9–418.7	0.2	10	36	200.2–300.0	0.2	10	27
419.2–618.7	0.5	12	45	300.5–500.0	0.5	10	30
619.2–818.7	0.5	12	51	500.5–700.0	0.5	12	39
819.7–1118.7	1	14	57	701–1000	1	14	45
1123.7–1318.7	5	14	60	1005–1200	5	14	51
1323.7–1618.7	5	14	66	1205–1500	5	14	54
1623.7–2118.7	5	16	75	1505–2000	5	16	63
2168.7–2568.7	50	18	81	2050–2450	50	18	69

Within the IOS approximation, we can express the integral cross section for a transition $n_1 j_1 j_2 \rightarrow n'_1 j'_1 j'_2$ out of the $n_{1,j_1} = 1_0$ fine-structure level. For collisions induced by H_2 , we detail two cases. These are treated in a pure Hund's case (b) even if the intermediate coupling is used for the calculations of the CC cross sections.

B.1. para- H_2

Setting $n_1 = 1$, $j_1 = 0$ and $j_2 = 0$ in (B.1) gives

$$\sigma_{100 \rightarrow n'_1 j'_1 j'_2} = 3[n'_1 j'_1 j'_2] \sum_{\lambda_1 \lambda_2 \lambda} \begin{pmatrix} n'_1 & \lambda_1 & 1 \\ 0 & 0 & 0 \end{pmatrix}^2 \times \begin{pmatrix} j'_2 & \lambda_2 & 0 \\ 0 & 0 & 0 \end{pmatrix}^2 \left\{ \begin{matrix} 0 & 1 & S \\ n'_1 & j'_1 & \lambda_1 \end{matrix} \right\}^2 \sigma_{\lambda_1 \lambda_2 \lambda}. \quad (\text{B.3})$$

It is possible to see that by setting $n'_1 = \lambda_1 + 1$, the 3j and 6j coefficients are nonzero for $j'_1 = \lambda_1$ and $j'_2 = \lambda_2$ so that

$$\sigma_{100 \rightarrow \lambda_1 + 1, \lambda_1, \lambda_2} = 3[\lambda_1 + 1][\lambda_1 \lambda_2] \begin{pmatrix} \lambda_1 + 1 & \lambda_1 & 1 \\ 0 & 0 & 0 \end{pmatrix}^2 \times \begin{pmatrix} \lambda_2 & \lambda_2 & 0 \\ 0 & 0 & 0 \end{pmatrix}^2 \left\{ \begin{matrix} 0 & 1 & S \\ \lambda_1 + 1 & \lambda_1 & \lambda_1 \end{matrix} \right\}^2 \times \sigma_{\lambda_1 \lambda_2 \lambda}. \quad (\text{B.4})$$

It should be noted that an equivalent set of equations like (B.4) can be found for $n'_1 = \lambda_1 - 1$. In the following and for the determination of the hyperfine rate coefficients, we chose to use the case where $n'_1 = \lambda_1 + 1$. The evaluation of the 3j and 6j coefficients in (B.4) leads to the expression for $\sigma_{\lambda_1 \lambda_2 \lambda}$:

$$\sigma_{\lambda_1 \lambda_2 \lambda} = \frac{[\lambda_1]}{\lambda_1 + 1} \sigma_{100 \rightarrow \lambda_1 + 1, \lambda_1, \lambda_2}. \quad (\text{B.5})$$

This relation stands for $S = 1$. By reintroducing (B.5) into (B.1), we obtain the IOS cross section scaling relation out of the $n_{1,j_1} = 1_0$ in the case of a collision with para- H_2 :

$$\sigma_{n_1 j_1 j_2 \rightarrow n'_1 j'_1 j'_2}^{\text{IOS-p}} = [n_1 n'_1 j'_1 j'_2] \sum_{\lambda_1 \lambda_2} \frac{[\lambda_1]}{\lambda_1 + 1} \begin{pmatrix} n'_1 & \lambda_1 & n_1 \\ 0 & 0 & 0 \end{pmatrix}^2 \times \begin{pmatrix} j'_2 & \lambda_2 & j_2 \\ 0 & 0 & 0 \end{pmatrix}^2 \left\{ \begin{matrix} n'_1 & n_1 & \lambda_1 \\ j'_1 & j_1 & S \end{matrix} \right\}^2 \times \sigma_{100 \rightarrow \lambda_1 + 1, \lambda_1, \lambda_2}^{\text{CC}}, \quad (\text{B.6})$$

where the IOS cross section is replaced by the CC cross section. It is also possible to replace the cross section by the rate coefficient. The extension to hyperfine scattering calculation gives directly Eq. (9).

B.2. ortho- H_2

Similarly, by applying $n_1 = 1$, $j_1 = 0$ and $j_2 = 1$ in (B.1), we find

$$\sigma_{101 \rightarrow n'_1 j'_1 j'_2} = 3[n'_1 j'_1 j'_2] \sum_{\lambda_1 \lambda_2 \lambda} \begin{pmatrix} n'_1 & \lambda_1 & 1 \\ 0 & 0 & 0 \end{pmatrix}^2 \times \begin{pmatrix} j'_2 & \lambda_2 & 1 \\ 0 & 0 & 0 \end{pmatrix}^2 \left\{ \begin{matrix} 0 & 1 & S \\ n'_1 & j'_1 & \lambda_1 \end{matrix} \right\}^2 \sigma_{\lambda_1 \lambda_2 \lambda}. \quad (\text{B.7})$$

In this case, for $n'_1 = \lambda_1 + 1$, the 3j and 6j coefficients give a contribution for $j'_1 = \lambda_1$ and $j'_2 = \lambda_2 + 1$. Replacing in (B.7), we find

$$\sigma_{101 \rightarrow \lambda_1 + 1, \lambda_1, \lambda_2 + 1} = 3[\lambda_1 + 1, \lambda_1, \lambda_2 + 1] \begin{pmatrix} \lambda_1 + 1 & \lambda_1 & 1 \\ 0 & 0 & 0 \end{pmatrix}^2 \times \begin{pmatrix} \lambda_2 + 1 & \lambda_2 & 1 \\ 0 & 0 & 0 \end{pmatrix}^2 \left\{ \begin{matrix} 0 & 1 & S \\ \lambda_1 + 1 & \lambda_1 & \lambda_1 \end{matrix} \right\}^2 \times \sigma_{\lambda_1 \lambda_2 \lambda}. \quad (\text{B.8})$$

The 3j and 6j coefficients in (B.8) are analyzed so that the expression for $\sigma_{\lambda_1 \lambda_2 \lambda}$ becomes

$$\sigma_{\lambda_1 \lambda_2 \lambda} = \frac{[\lambda_1]}{\lambda_1 + 1} \frac{[\lambda_2]}{\lambda_2 + 1} \sigma_{101 \rightarrow \lambda_1 + 1, \lambda_1, \lambda_2 + 1}. \quad (\text{B.9})$$

We can reintroduce (B.9) into (B.1) and obtain the IOS cross section scaling relation out of the $n_{1,j_1} = 1_0$ in the case of a collision with ortho- H_2 :

$$\sigma_{n_1 j_1 j_2 \rightarrow n'_1 j'_1 j'_2}^{\text{IOS-o}} = [n_1 n'_1 j'_1 j'_2] \sum_{\lambda_1 \lambda_2} \frac{[\lambda_1]}{\lambda_1 + 1} \frac{[\lambda_2]}{\lambda_2 + 1} \begin{pmatrix} n'_1 & \lambda_1 & n_1 \\ 0 & 0 & 0 \end{pmatrix}^2 \times \begin{pmatrix} j'_2 & \lambda_2 & j_2 \\ 0 & 0 & 0 \end{pmatrix}^2 \left\{ \begin{matrix} n'_1 & n_1 & \lambda_1 \\ j'_1 & j_1 & S \end{matrix} \right\}^2 \times \sigma_{101 \rightarrow \lambda_1 + 1, \lambda_1, \lambda_2 + 1}^{\text{CC}}. \quad (\text{B.10})$$

Similarly to the case of para- H_2 the extension to hyperfine scattering calculation is given by Eq. (10).

Appendix C: Details about fine-structure Einstein coefficients

For an open-shell molecule following the coupling scheme given in Sect. 3.1, the general form of the Einstein coefficient is given by (see, e.g., Sobelman 1979)

$$A_{n_1 j_1 \rightarrow n'_1 j'_1} = \frac{64\pi^4 \nu^3}{3hc^3} \frac{S'_{n_1 j_1 \rightarrow n'_1 j'_1}}{[j_1]}, \quad (\text{C.1})$$

$$S'_{n_1 j_1 \rightarrow n'_1 j'_1} = [j_1 j'_1] \left\{ \begin{matrix} n_1 & j_1 & S \\ j'_1 & n'_1 & 1 \end{matrix} \right\}^2 S'_{n_1 \rightarrow n'_1},$$

where ν is the frequency of the transition, h is the Planck constant, c is the speed of light, and $S'_{n_1 j_1 \rightarrow n'_1 j'_1}$ and $S'_{n_1 \rightarrow n'_1}$ are the line strength factors for a fine-structure and a rotational transition, respectively. The $S'_{n_1 \rightarrow n'_1}$ term depends on the electric dipole moment matrix elements, which allow transitions for $\Delta n_1 = \pm 1$ (Axner et al. 2004). It turns out that

$$S'_{n_1 \rightarrow n'_1} = \mu_D^2 \max(n_1, n'_1) = \mu_D^2 n_1. \quad (\text{C.2})$$

Reintroduce (C.2) into (C.1) simplifies to

$$A_{n_1 j_1 \rightarrow n'_1 j'_1} = \frac{64\pi^4 \nu^3}{3hc^3} \mu_D^2 n_1 [j_1] \left\{ \begin{matrix} n_1 & j_1 & S \\ j'_1 & n'_1 & 1 \end{matrix} \right\}^2. \quad (\text{C.3})$$

In the case of NH and ND, $S = 1$ and $\mu_D = 1.39$ D (Keun Park & Sun 1993).